

Model-Predictive Trajectory Generation for Autonomous Aerial Search and Coverage

Hugo Matias, Daniel Silvestre

Abstract—This paper addresses the trajectory planning problem for search and coverage missions with an Unmanned Aerial Vehicle (UAV). The objective is to devise optimal coverage trajectories based on a utility map describing prior region information, assumed to be effectively approximated by a Gaussian Mixture Model (GMM). We introduce a Model Predictive Control (MPC) algorithm employing a relaxed formulation that promotes the exploration of the map by preventing the UAV from revisiting previously covered areas. This is achieved by penalizing intersections between the UAV’s visibility regions along its trajectory. The algorithm is assessed in MATLAB and validated in Gazebo, as well as in outdoor experimental tests. The results demonstrate the efficacy of the proposed strategy in generating efficient and smooth trajectories for search and coverage missions.

Index Terms—Unmanned Aerial Vehicles, Trajectory Planning, Model Predictive Control, Gaussian Mixture Models.

I. INTRODUCTION

DRONES, or Unmanned Aerial Vehicles (UAVs), are an emerging technology with significant potential, offering a range of applications across various sectors. These versatile aerial platforms, often equipped with high-resolution cameras, sensors, and cutting-edge technology, have the capacity to perform operations autonomously, reducing the need for constant human intervention [1], [2]. Notably, drones are particularly valuable for search and coverage missions, given their ability to cover extensive regions with unprecedented ease and speed. This kind of mission finds relevance in numerous applications, including search and rescue, wildfire prevention, surveillance, and mapping, among others [3]–[6].

In such a context, the main challenge involves devising trajectories to efficiently cover a designated region. This amounts to a complex decision-making and control problem, requiring consideration of several factors, including mission objectives, vehicle dynamics, and time constraints. Particularly, we focus on the coverage problem based on a utility map describing prior region information. Thus, the coverage mission can be modeled as an Optimal Control Problem (OCP) that involves planning dynamically feasible trajectories, which should maximize the utility volume covered by the sensor footprint within limited flight time.

H. Matias (hugomatas@tecnico.ulisboa.pt) is with the Institute for Systems and Robotics, Instituto Superior Técnico, University of Lisbon, Portugal.

D. Silvestre (dsilvestre@isr.tecnico.ulisboa.pt) is with the School of Science and Technology from the NOVA University of Lisbon, Portugal, with COPELABS from the Lusófona University, and also with the Institute for Systems and Robotics, Instituto Superior Técnico, University of Lisbon.

This work was partially supported by the Portuguese Fundação para a Ciência e a Tecnologia (FCT) through the Institute for Systems and Robotics (ISR), under Laboratory for Robotics and Engineering Systems (LARSyS) project UIDB/50009/2020, through project PCIF/MPG/0156/2019 FirePuma and through COPELABS, Lusofona University project UIDB/04111/2020.

Several approaches have been suggested in the literature, which can be categorized into two groups [7]. The first group comprises exhaustive strategies where the UAV systematically covers the target region. These methods are mainly geometric, i.e., the trajectory generation consists of generating geometric paths and subsequently parameterizing these paths over time. Common strategies include spiral patterns [8] and back-and-forth movements [9]. Additionally, graph-based methods, such as the A* algorithm [10], have also been applied to coverage problems. However, the exhaustive strategy is evidently inefficient when there are areas of no interest since the entire region is covered without any heuristic.

The second group aims to generate efficient coverage trajectories based on prior information about the region. Typical approaches consist of discretizing the target region into a grid and assigning a corresponding importance value to each grid cell. Subsequently, the trajectory generation process aims to prioritize the most important areas and is typically based on Bayesian-like updates. Numerous mathematical and heuristic techniques have been proposed, including greedy algorithms [11], probabilistic methods [12], and Mixed-Integer Programming (MIP) approaches [13]. A receding horizon approach has also been proposed in [14]. However, the trajectories are planned based on heuristics, and the method also requires the discretization of the space. Therefore, there is still no standard for an optimization-based solution to the problem.

This work introduces a trajectory planning algorithm for search and coverage missions with a UAV, based on a utility map described by a Gaussian Mixture Model (GMM). The proposed strategy, based on Model Predictive Control (MPC), adopts a formulation that promotes the exploration of the map by penalizing intersections between the visibility regions of the drone along its trajectory. It can produce efficient and smooth trajectories, accommodating both online and offline execution.

The remaining sections are organized as follows. We formulate the trajectory planning problem in Section II. Section III presents the proposed approach to the problem, and Section IV describes the control architecture used for implementing the devised algorithm in a quadrotor UAV. To show the efficacy of the proposed strategy, Section V provides illustrative examples obtained in MATLAB, and Section VI conducts further tests in Gazebo, along with experiments in an outdoor environment. Section VII summarizes conclusions and future directions.

Notation: We denote the set of integers from i to j as $\mathbb{Z}_{[i,j]}$. Also, $\mathbf{0}_{m \times n}$ and $\mathbf{1}_{m \times n}$ denote, respectively, the matrices of zeros and ones with dimension $m \times n$, and \mathbf{I}_n is the identity matrix of size n . The set of positive-definite matrices of size n is denoted as $\mathbb{R}_{>0}^{m \times n}$.

II. PRELIMINARIES & PROBLEM FORMULATION

This section formalizes mathematically the trajectory planning problem addressed in this paper. It begins by establishing assumptions concerning the utility map, denoted as an uncertainty map, and the sensing model of the UAV. Subsequently, we formulate the problem from an optimal control standpoint.

A. Uncertainty Map

The uncertainty map is a nonnegative function $h : \mathbb{R}^2 \rightarrow \mathbb{R}_0^+$ that describes the prior significance of each point $\mathbf{p} \in \mathbb{R}^2$ to be analyzed by the vehicle. Since the original structure of the uncertainty map typically may not follow common and well-known models, we assume that the uncertainty function can be arbitrarily well approximated by a GMM, which is a weighted sum of Gaussian components. More specifically, for a model with M components, the uncertainty map is given by

$$h(\mathbf{p}) = \sum_{i=1}^M w_i \mathcal{N}(\mathbf{p}; \boldsymbol{\mu}_i, \boldsymbol{\Sigma}_i), \quad \forall \mathbf{p} \in \mathbb{R}^2, \quad (1)$$

where each component \mathcal{N} is a conventional two-dimensional Gaussian distribution. The parameters $w_i \in \mathbb{R}_0^+$, $\boldsymbol{\mu}_i \in \mathbb{R}^2$, and $\boldsymbol{\Sigma}_i \in \mathbb{R}_{>0}^{2 \times 2}$ are, respectively, the weight, the mean vector, and the covariance matrix of the i th Gaussian component. Additionally, we highlight that the uncertainty map is not required to be a Probability Density Function (PDF). Nevertheless, for convenience, we assume that the map is normalized, meaning that the prior uncertainty volume is one and, therefore, the weights verify $\sum_{i=1}^M w_i = 1$. Fig. 1 illustrates a plausible instance of an uncertainty map.

B. Sensing Model

This work assumes that the drone flies at a constant altitude and features a gimbal camera, which remains directed downwards even when the vehicle performs pitch or roll maneuvers. Moreover, at each time instant t , we assume the camera covers a circular region, $\mathcal{B}_r(\mathbf{p}_c)$, defined by

$$\mathcal{B}_r(\mathbf{p}_c) \triangleq \{\mathbf{p} \in \mathbb{R}^2 : \|\mathbf{p} - \mathbf{p}_c\| < r\}, \quad (2)$$

where $\mathbf{p}_c \in \mathbb{R}^2$ is the vehicle's horizontal position and r is the observation radius, which depends on the camera's Field of View (FOV) and the altitude, as displayed in Fig. 2. In addition, the vehicle is assumed to have a perfect quality of exploration, meaning that after it analyzes a given area, the uncertainty reduces to zero for all points inside the observation radius and there is no reward for revisiting the same region.

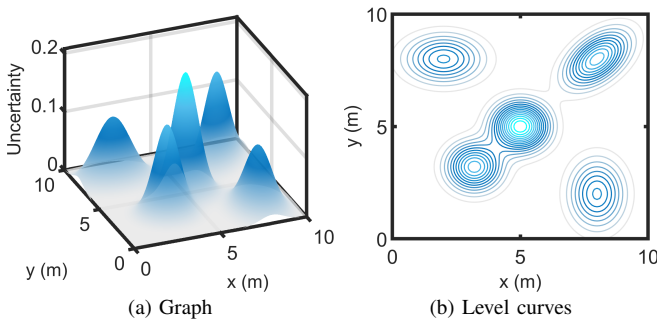


Fig. 1: Example of an uncertainty map comprising five Gaussian components.

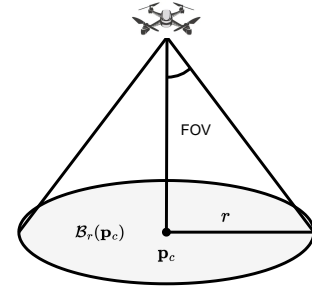


Fig. 2: Sensor FOV and visibility region.

C. Optimal Control Problem

The problem addressed in this letter amounts to generating optimal trajectories that guide the UAV. The trajectories should maximize an objective functional regarding the mission goals while satisfying constraints accounting for their dynamic feasibility. Consequently, this problem can be formulated as the following OCP

$$\begin{aligned} & \underset{\mathbf{x}, \mathbf{u}}{\text{maximize}} && J(\mathbf{x}, \mathbf{u}) \\ & \text{subject to} && \mathbf{x}(0) = \mathbf{x}_0, \\ & && \dot{\mathbf{x}}(t) = \mathbf{F}(\mathbf{x}(t), \mathbf{u}(t)), \quad \forall t \in [0, T], \\ & && \mathbf{x}(t) \in \mathcal{X}, \quad \forall t \in [0, T], \\ & && \mathbf{u}(t) \in \mathcal{U}, \quad \forall t \in [0, T], \end{aligned} \quad (3)$$

where T denotes the total flight duration, $\mathbf{x} : [0, T] \rightarrow \mathbb{R}^{n_x}$ and $\mathbf{u} : [0, T] \rightarrow \mathbb{R}^{n_u}$ designate the state and input signals of the vehicle's model described by an Ordinary Differential Equation (ODE), and \mathbf{x}_0 is the initial state. Furthermore, the sets \mathcal{X} and \mathcal{U} constitute the admissible states and inputs for the vehicle, which are derived from limits imposed by vehicle dynamics and the surrounding environment.

Let $\gamma : [0, T] \rightarrow \mathbb{R}^2$ denote the vehicle's trajectory, related to the state through an auxiliary matrix $\mathbf{C}_\gamma \in \mathbb{R}^{2 \times n_x}$,

$$\gamma(t) = \mathbf{C}_\gamma \mathbf{x}(t), \quad \forall t \in [0, T]. \quad (4)$$

The objective is to maximize the uncertainty reduction, i.e., the difference between the uncertainty volume in the map before and after the autonomous mission. Therefore, considering the previous assumptions, the objective functional J is given by

$$J(\gamma) = \int_{\mathcal{C}_r(\gamma)} h(\mathbf{p}) d\mathbf{p}, \quad (5)$$

where the set $\mathcal{C}_r(\gamma)$ is defined as the union of all observation circles along the trajectory of the vehicle,

$$\mathcal{C}_r(\gamma) \triangleq \bigcup_{t=0}^T \mathcal{B}_r(\gamma(t)), \quad (6)$$

as illustrated in Fig. 3. The usefulness of the set $\mathcal{C}_r(\gamma)$ arises from the fact that each position is only integrated once since we assume the vehicle has a perfect quality of exploration.

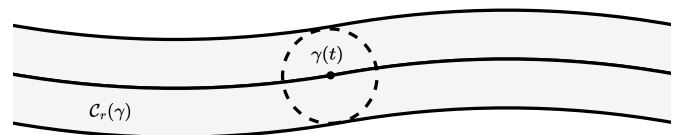


Fig. 3: Illustration of the set $\mathcal{C}_r(\gamma)$.

Solving the optimal control problem in (3) is very complex since the objective functional J , as defined in (5), does not have a closed-form expression. Therefore, a relaxed formulation needs to be considered. In addition, to make the problem computationally tractable, it needs to be discretized as well. However, even after relaxing and discretizing the problem, solving the problem globally for a relatively large flight time T is computationally challenging. Consequently, we consider a local approach based on MPC with a relaxed formulation to approximate the solutions of (3) while adding the possibility for feedback to the control law.

III. MODEL-PREDICTIVE APPROACH WITH RELAXED FORMULATION

To tackle the problem outlined in the previous section, we employ a local approximation based on MPC with a relaxed formulation of the objective function. MPC consists in solving a discrete-time OCP at each sampling time. Each optimization results in a sequence of future optimal control actions and a corresponding sequence of future states. Only the first sample from the predicted optimal control sequence is applied to the vehicle, and then the process repeats at the next sampling time.

More specifically, at each discrete-time instant k , for a given initial state $\mathbf{x}[k]$ of the vehicle, the control policy is defined by solving an optimization problem of the form

$$\begin{aligned} & \underset{\hat{\mathbf{x}}_k, \hat{\mathbf{u}}_k}{\text{maximize}} && J_k(\hat{\mathbf{x}}_k, \hat{\mathbf{u}}_k) \\ & \text{subject to} && \hat{\mathbf{x}}_k[0] = \mathbf{x}[k], \\ & && \hat{\mathbf{x}}_k[n+1] = \mathbf{f}(\hat{\mathbf{x}}_k[n], \hat{\mathbf{u}}_k[n]), \quad \forall n \in \mathbb{Z}_{[0, N-1]}, \\ & && \hat{\mathbf{x}}_k[n] \in \mathcal{X}, \quad \forall n \in \mathbb{Z}_{[0, N]}, \\ & && \hat{\mathbf{u}}_k[n] \in \mathcal{U}, \quad \forall n \in \mathbb{Z}_{[0, N-1]}, \end{aligned} \quad (7)$$

where N is the prediction horizon length, $\hat{\mathbf{x}}_k : \mathbb{Z}_{[0, N]} \rightarrow \mathbb{R}^{n_x}$ and $\hat{\mathbf{u}}_k : \mathbb{Z}_{[0, N-1]} \rightarrow \mathbb{R}^{n_u}$ designate the predicted state and control sequences at time instant k , and function \mathbf{f} describes a discretized model of the vehicle dynamics. Moreover, the sets \mathcal{X} and \mathcal{U} constitute the admissible states and inputs for the vehicle, as defined in (3). The input applied to the vehicle at discrete-time instant k , $\mathbf{u}[k]$, is given by

$$\mathbf{u}[k] = \hat{\mathbf{u}}_k^*[0], \quad (8)$$

where $\hat{\mathbf{u}}_k^*[0]$ is the first action of the predicted optimal control sequence at discrete-time instant k . In a general sense, the optimization problem defined in (7) is a structured Nonlinear Program (NLP), which may be solved efficiently using commercially available NLP solvers.

A. Objective Function

Our approach for approximating the problem described in Section II relies on a relaxed formulation of the MPC objective function. More precisely, the objective function is defined as a combination of two objectives as

$$J_k(\hat{\gamma}_k) = \tilde{J}_k(\hat{\gamma}_k) - \lambda P_k(\hat{\gamma}_k), \quad (9)$$

where $\hat{\gamma}_k : \mathbb{Z}_{[0, N]} \rightarrow \mathbb{R}^2$ is the predicted sequence of vehicle positions at discrete-time instant k , such that $\hat{\gamma}_k[n] = \mathbf{C}\hat{\mathbf{x}}_k[n]$, $\forall n \in \mathbb{Z}_{[0, N]}$, and $\lambda \in \mathbb{R}_0^+$ is a scaling coefficient that weighs the relative importance of the two objectives.

The first term in (9), \tilde{J}_k , expresses the objective of prioritizing the regions with the highest uncertainty. Namely, it is determined by summing the uncertainty volumes that are predicted to be covered by the vehicle at each time instant of the prediction horizon,

$$\tilde{J}_k(\hat{\gamma}_k) = \sum_{n=0}^N \int_{\mathcal{B}_r(\hat{\gamma}_k[n])} h(\mathbf{p}) d\mathbf{p}. \quad (10)$$

Nevertheless, this term alone does not consider the previously covered regions nor the intersections between the observation areas within the prediction horizon. Consequently, if the objective function was defined only by such a term, the resulting trajectories would converge to a point where the uncertainty volume covered by the vehicle is maximum (at least locally) and remain at that point.

To contemplate the information on the previously explored regions along with the intersections between the observation areas within the prediction horizon, we add a penalty term P_k to the MPC objective function. This term penalizes intersections between all possible pairs of observation circles along the vehicle's trajectory. Thus, two kinds of intersections can be distinguished: intersections between the predicted observation circles and previously covered ones, and intersections between the observation circles over the prediction horizon. Hence, the penalty term can be written as

$$P_k(\hat{\gamma}_k) = P_k^B(\hat{\gamma}_k) + P_k^H(\hat{\gamma}_k), \quad (11)$$

where P_k^B penalizes intersections between the predicted observation circles and previously covered circles, and P_k^H penalizes intersections within the prediction horizon. Therefore, assuming that $p : \mathbb{R}^2 \times \mathbb{R}^2 \rightarrow \mathbb{R}_0^+$ is a function that penalizes the intersection between two circles and $\gamma[i]$ is the vehicle's position at discrete-time instant i , P_k^B is defined as

$$P_k^B(\hat{\gamma}_k) = \sum_{n=1}^N \sum_{i=0}^k p(\hat{\gamma}_k[n], \gamma[i]), \quad (12)$$

and P_k^H is given by

$$P_k^H(\hat{\gamma}_k) = \sum_{n=2}^N \sum_{i=1}^{n-1} p(\hat{\gamma}_k[n], \hat{\gamma}_k[i]). \quad (13)$$

To clarify the proposed methodology, Fig. 4 visually represents the previously covered regions and the regions predicted to be covered by the vehicle at a given iteration of the MPC algorithm. Now it remains to discuss how the penalty function p can be defined. We delve into this matter in the following subsection.

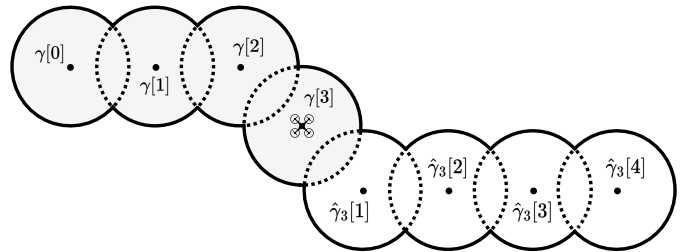


Fig. 4: Illustration of the observation regions at discrete-time instant $k = 3$ for a prediction horizon length of $N = 4$ (grey - previously covered circles; white - predicted observation circles).

Before proceeding, it is worth highlighting that the integral evaluations in (10) still cannot be expressed in closed form. Nevertheless, as the integrals are now computed over circular domains, it becomes possible to approximate them through numerical methods such as quadrature rules or by discretizing the observation area using a grid. However, we will typically focus on scenarios where the observation radius is small compared to the structure of the uncertainty map. Consequently, (10) can be effectively approximated by

$$\tilde{J}_k(\hat{\gamma}_k) \simeq \pi r^2 \sum_{n=0}^N h(\hat{\gamma}_k[n]). \quad (14)$$

B. Penalty Function

A plausible way to construct the penalty function p could be to define it as the overlap area between two circles, which can be computed analytically. Let $\mathbf{c}_1, \mathbf{c}_2 \in \mathbb{R}^2$ denote the centers of two circles, both with radius r , and $d = \|\mathbf{c}_1 - \mathbf{c}_2\|$ the distance between them. The intersection area between the two circles, $a : \mathbb{R}_0^+ \rightarrow \mathbb{R}_0^+$, is given by

$$a(d) = \begin{cases} 2r^2 \arccos\left(\frac{d}{2r}\right) - d\sqrt{r^2 - d^2}, & \text{if } d \leq 2r, \\ 0, & \text{if } d > 2r. \end{cases} \quad (15)$$

However, an expression of such complexity would represent a computational bottleneck. Furthermore, the function in (15) is defined piecewise, posing additional implementation difficulties. For instance, the logic condition could be dealt with through the Big-M notation from YALMIP [15], which serves to convert the logic condition into a set of constraints using auxiliary binary variables and logic constraints.

Nevertheless, it is not necessary to accurately compute the overlap area between two circles to penalize the intersection between them. Instead, such penalization can be accomplished by creating a function that directly penalizes the existence of intersection. As a result, we formulate the penalty function by imposing an exponential penalty on the violation of the condition $\|\mathbf{c}_1 - \mathbf{c}_2\| > 2r$. More precisely, the penalty function is defined as

$$p(\mathbf{c}_1, \mathbf{c}_2) = \exp\left\{\alpha\left((2r)^2 - \|\mathbf{c}_1 - \mathbf{c}_2\|^2\right)\right\} - 1, \quad (16)$$

where $\alpha > 0$ is a parameter that can be tuned. Additionally, the subtraction of 1 is included so that the penalty function has a value of zero when $\|\mathbf{c}_1 - \mathbf{c}_2\| = 2r$, but it has no effect on the optimization since it is a constant term. Fig. 5 illustrates the evolution of the penalty function with the distance between the two circles for some values of α .

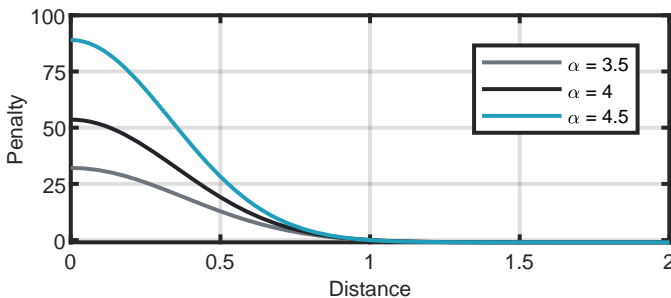


Fig. 5: Evolution of the penalty function with the distance between the two circles for some values of α while considering $r = 0.5$ m.

C. Computational Complexity

From a computational standpoint, it is significant to analyze the complexity of the proposed algorithm. Besides the inherent complexity of the problem, determined by the structure of the uncertainty map and the imposed restrictions, it is relevant to examine the number of terms comprising the MPC objective function, which directly influences the number of evaluations that the optimization solver must carry out. In particular, it is worth noting that the number of terms comprising \tilde{J}_k and P_k^H is determined by the prediction horizon length. Specifically, the number of terms in \tilde{J}_k increases linearly with the horizon length, whereas P_k^H consists of $N(N-1)/2$ terms, leading to a quadratic growth with respect to the horizon length.

Besides the quadratic growth of P_k^H as the horizon length increases, a significant computational burden arises from P_k^B . At each time instant k , the number of terms comprising P_k^B increases by N , meaning that P_k^B grows linearly with the flight time assigned for the surveillance mission. One apparent solution might involve defining a maximum backward horizon length N_B , thereby limiting P_k^B to a given number of terms. This consists in defining P_k^B as

$$P_k^B(\hat{\gamma}_k) = \sum_{n=1}^N \sum_{i=k-N_B+1}^k p(\hat{\gamma}_k[n], \gamma[i]). \quad (17)$$

Nonetheless, if the backward time horizon is not long enough, the vehicle may revisit previously explored regions. Hence, a more effective approach to be considered in future research consists of developing a subroutine capable of progressively reducing the number of components in the penalty term while preserving information about all previously covered regions.

Additionally, it is relevant to clarify that despite the notion that the number of terms in the objective function grows at each time step, the optimization solvers are built by allocating the necessary resources for the entire mission duration. This decision follows from the substantial additional overhead that there would be in generating a solver at each time step. Hence, the number of terms in the objective function actually remains constant throughout the whole mission, with the terms related to future time steps in P_k^B being assigned a null weight. As a result, despite potential fluctuations introduced by the problem, the computational times are expected to remain approximately constant during the surveillance mission.

D. Evaluation Metric

It is essential to establish an overall metric to evaluate the performance of the algorithm and perform comparisons. In this context, a reliable approach for assessing the quality of the generated trajectories involves computing the time evolution of the uncertainty volume covered by the vehicle. By disregarding the uncertainty coverage between sampling times, this metric can be approximated as

$$H_\gamma[k] = \int_{\bigcup_{i=0}^k \mathcal{B}_r(\gamma[i])} h(\mathbf{p}) d\mathbf{p}. \quad (18)$$

Furthermore, since there is no closed-form expression for (18), the metric is numerically approximated by discretizing the map into a grid.

IV. QUADROTOR MOTION CONTROL

This work focuses on multirotor aerial vehicles because of their agility and hovering capabilities. Moreover, a quadrotor is available to perform experimental tests. Consequently, this section outlines the control architecture employed to implement the proposed algorithm on a quadrotor aerial vehicle.

We consider a dual-layer structure of motion control, as illustrated in Fig. 6. The proposed MPC algorithm serves as the higher-level controller (trajectory planner), which generates high-level references for the UAV. The lower-level controller (trajectory tracker) directly applies control inputs to the vehicle to accurately track the references provided by the upper-level controller. For the purpose of efficiency, the MPC algorithm considers a simplified model of the vehicle, while the lower-level controller accounts for the full quadrotor dynamics.

A. Full Dynamics Model

For completeness, we begin by describing the full nonlinear dynamics of a quadrotor. The nonlinear quadrotor dynamics are described in the body $\{B\}$ and inertial $\{I\}$ frames depicted in Fig. 7 while assuming that the origin of $\{B\}$ is coincident with the quadrotor's center of mass. Let $\xi \triangleq [\gamma \ z]^\top$ denote the quadrotor's position in the inertial frame and $\eta \triangleq [\phi \ \theta \ \psi]^\top$ describe the orientation of the body frame with respect to the inertial frame, where ϕ , θ and ψ are the roll, pitch and yaw angles. Moreover, let $\omega \in \mathbb{R}^3$ denote the angular velocity of $\{B\}$ with respect to $\{I\}$, expressed in $\{B\}$. Additionally, let $\mathbf{R}(\eta) \in SO(3)$ be the rotation matrix from $\{B\}$ to $\{I\}$ and $\mathbf{T}(\eta) \in \mathbb{R}^{3 \times 3}$ a matrix that converts the angular velocity to angle rates. Finally, let m be the mass of the vehicle, $\mathbf{I} \in \mathbb{R}^{3 \times 3}$ the inertia matrix expressed in $\{B\}$, and g the gravitational acceleration. The quadrotor equations of motion, based on the Newton-Euler formalism [16], are given by

$$\begin{aligned} m\ddot{\xi} &= -mge_3 + \mathbf{R}(\eta) Fe_3, \\ \dot{\eta} &= \mathbf{T}(\eta) \omega, \\ \mathbf{I}\dot{\omega} &= -\omega \times \mathbf{I}\omega + \tau, \end{aligned} \quad (19)$$

where F is the net thrust and $\tau \in \mathbb{R}^3$ is the vector of moments applied to the UAV, described in $\{B\}$. Ultimately, the relation between the rotation speeds of the rotors, $\bar{\omega}_i$, $i = 1, \dots, 4$, and the thrust and moment vector can be modeled as

$$\begin{bmatrix} F \\ \tau \end{bmatrix} = \Gamma \begin{bmatrix} \bar{\omega}_1^2 \\ \bar{\omega}_2^2 \\ \bar{\omega}_3^2 \\ \bar{\omega}_4^2 \end{bmatrix}, \quad (20)$$

where $\Gamma \in \mathbb{R}^{4 \times 4}$ is a matrix dependant on the rotors arrangement relative to the quadrotor's center of mass and on aerodynamic constants, which may be determined experimentally. Additional complex aerodynamic effects are neglected.

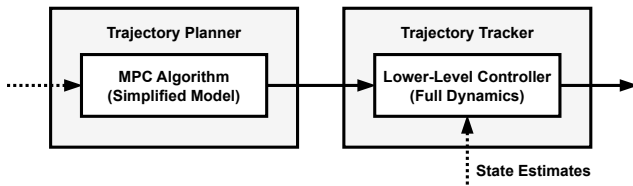


Fig. 6: Full motion control scheme of the UAV.

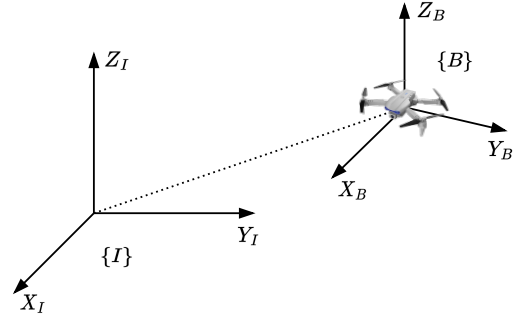


Fig. 7: Quadrotor reference frames.

B. Simplified Model

At the planning level, considering that the UAV flies at a constant altitude and ignoring the fast rotational dynamics of the vehicle, the UAV might be modeled as a two-dimensional point-mass system with double-integrator dynamics. Thus, the state vector is composed of the positions and velocities on the horizontal plane, $\mathbf{x} = [\gamma^\top \ \dot{\gamma}^\top]^\top$, and the control input is the acceleration on the horizontal plane. Consequently, at the planning level, the quadrotor dynamics take the linear form

$$\begin{bmatrix} \dot{\gamma} \\ \ddot{\gamma} \end{bmatrix} = \begin{bmatrix} \mathbf{0}_{2 \times 2} & \mathbf{I}_{2 \times 2} \\ \mathbf{0}_{2 \times 2} & \mathbf{0}_{2 \times 2} \end{bmatrix} \begin{bmatrix} \gamma \\ \dot{\gamma} \end{bmatrix} + \begin{bmatrix} \mathbf{0}_{2 \times 2} \\ \mathbf{I}_{2 \times 2} \end{bmatrix} \mathbf{u}, \quad (21)$$

where $\mathbf{0}_{2 \times 2}$ denotes a matrix of zeros and $\mathbf{I}_{2 \times 2}$ denotes the identity matrix, both with dimension 2×2 . Such a mismatch is not critical for obtaining good performance in real conditions as long as the generated trajectories are not extremely aggressive so that the inner-loop dynamics become visible.

C. Implementation Details

In practical terms, the proposed motion control scheme is implemented using a PX4 Autopilot [17]. The PX4 Autopilot provides the lower-level controller and an Extended Kalman Filter (EKF) to process sensor measurements and provide state estimates to the controllers. As detailed in Fig. 8, the controller supplied by the PX4 Autopilot follows a standard cascaded architecture with several stages. Each stage is composed of a proportional or Proportional-Integral-Derivative (PID) controller that generates references for the upcoming stage based on references provided by the previous stage. From a general perspective, the PX4 controller consists of two main control loops: position and attitude. The position control loop commands accelerations, which are then converted into attitude and net thrust references. The attitude control loop receives attitude and net thrust references and commands thrust references for the vehicle motors. With such an architecture, the PX4 controller is able to receive different kinds of references.

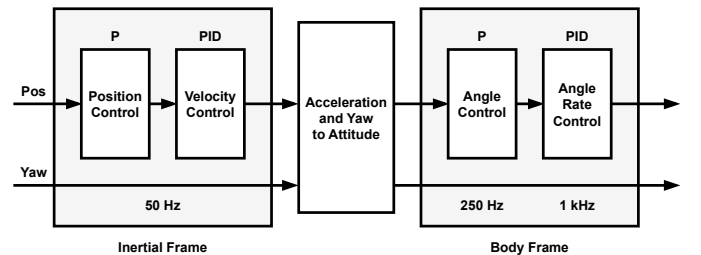


Fig. 8: PX4 controller architecture (adapted from PX4 documentation).

V. SIMULATION RESULTS

In this section, the efficacy of the proposed MPC algorithm is assessed through different simulation examples obtained in a MATLAB environment. The goal is to perform an initial analysis of the proposed MPC algorithm. Therefore, the simulations presented in this section are performed assuming that the UAV follows ideal double-integrator dynamics with constraints on the maximum velocity and acceleration magnitudes. At each discrete-time instant k , the MPC algorithm involves solving the following optimization problem

$$\begin{aligned} & \underset{\hat{\mathbf{x}}_k, \hat{\mathbf{u}}_k}{\text{maximize}} && J_k(\hat{\mathbf{x}}_k, \hat{\mathbf{u}}_k) \\ & \text{subject to} && \hat{\mathbf{x}}_k[0] = \mathbf{x}[k], \\ & && \hat{\mathbf{x}}_k[n+1] = \mathbf{A}\hat{\mathbf{x}}_k[n] + \mathbf{B}\hat{\mathbf{u}}_k[n], \quad \forall n \in \mathbb{Z}_{[0, N-1]}, \\ & && \|\mathbf{C}_\gamma \hat{\mathbf{x}}_k[n]\| \leq v_{\max}, \quad \forall n \in \mathbb{Z}_{[0, N]}, \\ & && \|\hat{\mathbf{u}}_k[n]\| \leq a_{\max}, \quad \forall n \in \mathbb{Z}_{[0, N-1]}, \end{aligned} \quad (22)$$

where the objective function J_k is obtained as described in Section III. The matrices \mathbf{A} and \mathbf{B} correspond to the discrete double-integrator dynamics (zero-order hold) and are given as

$$\mathbf{A} = \begin{bmatrix} \mathbf{I}_{2 \times 2} & T_s \mathbf{I}_{2 \times 2} \\ \mathbf{0}_{2 \times 2} & \mathbf{I}_{2 \times 2} \end{bmatrix}, \quad \mathbf{B} = \begin{bmatrix} T_s^2/2 \mathbf{I}_{2 \times 2} \\ T_s \mathbf{I}_{2 \times 2} \end{bmatrix}, \quad (23)$$

where T_s stands for the sampling period. In addition, the auxiliary matrix $\mathbf{C}_\gamma = [\mathbf{0}_{2 \times 2} \quad \mathbf{I}_{2 \times 2}]$ extracts the velocity from the state, and v_{\max} and a_{\max} denote, respectively, the maximum velocity and acceleration that the vehicle may achieve.

The simulation results presented in this section were obtained in MATLAB using the CasADi [18] optimization modeling toolbox, along the IPOPT [19] solver. At each sampling time, the solution obtained at the previous step was used to set the initial guess for the current step by performing the shifting warm-start method (see e.g. [20]). All computations were executed on a single desktop computer with an Intel Core i7-6700K @ 4.00 GHz processor and 32.00 GB of RAM.

A. Illustrative Examples

We begin by presenting some illustrative examples to showcase the trajectories that the algorithm is able to produce for different uncertainty maps. In such examples, the drone starts at the position $\mathbf{p} = [1 \ 1]^\top$ [m] with no initial velocity, and the radius of observation is assumed to be $r = 1$ m. The sampling period is $T_s = 0.1$ s, the horizon is $N = 15$, and the vehicle has a max velocity of 4 m/s and a max acceleration of 4 m/s².

In the first example, illustrated in Fig. 9, the uncertainty map is composed of a single radially symmetric component. As shown in Fig. 9 (a), initially the vehicle moves towards the maximizer of the Gaussian component. Subsequently, as a result of the penalties applied by the algorithm, the vehicle moves to wider regions by executing a spiral curve with the temporal profiles depicted in Figs. 9 (c) and 9 (e), respectively. Also, Fig. 9 (b) illustrates the sensor footprint of the UAV, and Fig. 9 (d) shows the accumulation of the uncertainty volume covered by the vehicle over time. In addition, we draw attention to Fig. 9 (f), which presents the mean solver times acquired through 100 simulations, with each iteration taking approximately 8 ms on average.

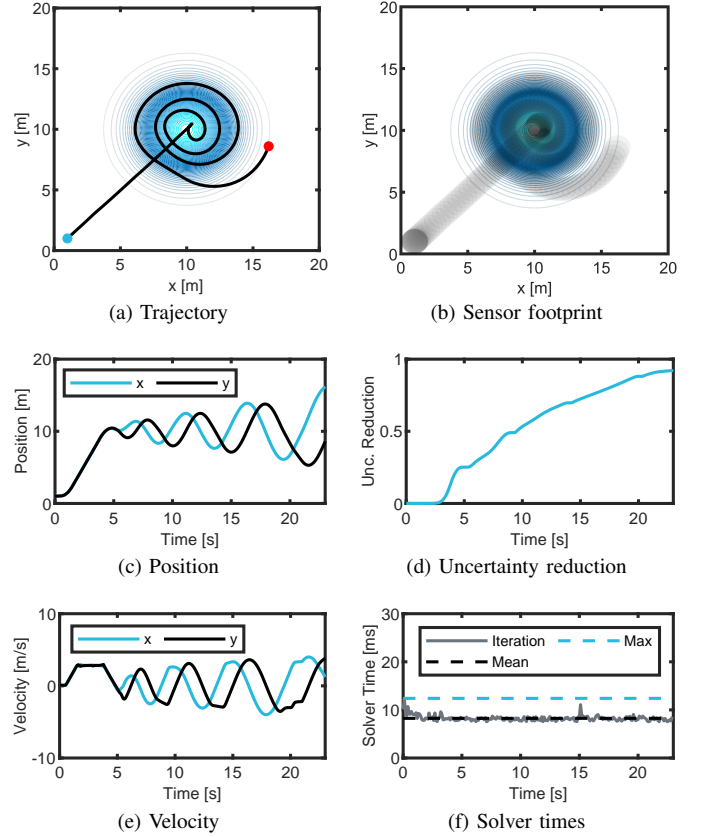


Fig. 9: Simple simulation with a single radially symmetric component.

In Fig. 10, we introduce another simple simulation in which the uncertainty map consists of a single Gaussian component but now with an elliptical shape. In such a case, the trajectory adjusts itself to the elliptical shape of the Gaussian component, as can be observed in Fig. 10 (a). Furthermore, as shown in Figs. 10 (c) and 10 (d), the resulting position and uncertainty reduction profiles are similar to those from the previous example. There is also no noticeable change in the computational times when compared to the first example.

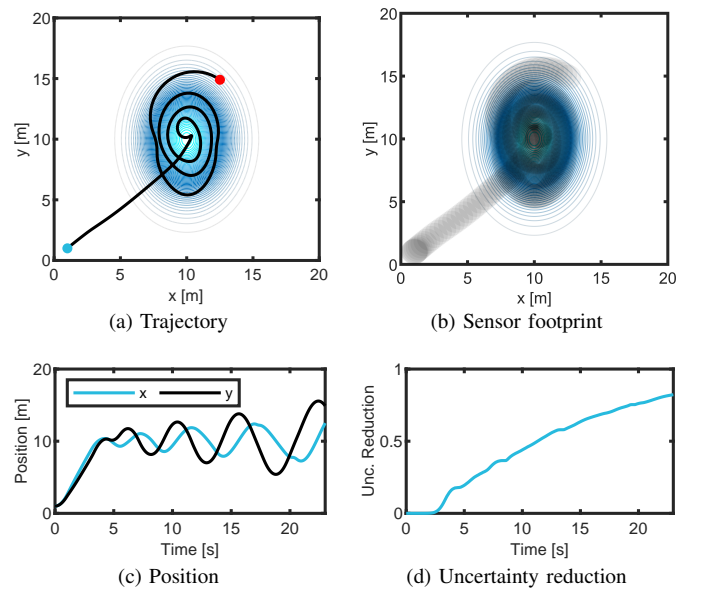


Fig. 10: Simple simulation with a single component with an elliptical shape.

Now, we consider a more complex example in which the uncertainty function consists of three Gaussian components, with the corresponding results displayed in Fig. 11. As depicted in Fig. 11 (a), the drone analyzes each component individually. Notably, the components with means at positions $\mathbf{p} = [15 \ 5]^\top$ and $\mathbf{p} = [10 \ 15]^\top$ exhibit similarities to those in the previous examples, and the observed trajectories align with the previous patterns. However, the third component located at $\mathbf{p} = [5 \ 5]^\top$ has a smaller variance when compared to the observation radius of the UAV. Consequently, when the drone analyzes this component, it simply hovers at the component's maximizer. Additionally, we highlight that the computational times are slightly higher in this example, with each iteration averaging approximately 12 ms.

Ultimately, we introduce an example where the uncertainty map is composed of four radially symmetric Gaussian components, with the corresponding simulation results displayed in Fig. 12. As it can be observed in Fig. 12 (a), the component with mean at $\mathbf{p} = [5 \ 5]^\top$ is similar to the one from the previous example, and the vehicle exhibits a similar behavior when analyzing this component. The remaining components with means at $\mathbf{p} = [5 \ 15]^\top$, $\mathbf{p} = [15 \ 15]^\top$ and $\mathbf{p} = [15 \ 5]^\top$ all have similar covariance matrices but different associated weights. By observing Figs. 12 (a) and 12 (b), one can notice that, as the weights of the components increase, the spiral curves become more tightly concentrated, and there is a greater overlap of the vehicle's observation circles. In addition, we highlight that, in this example, the computational times are rather higher, with each solver iteration taking approximately 16 ms on average, as shown in Fig. 12 (f).

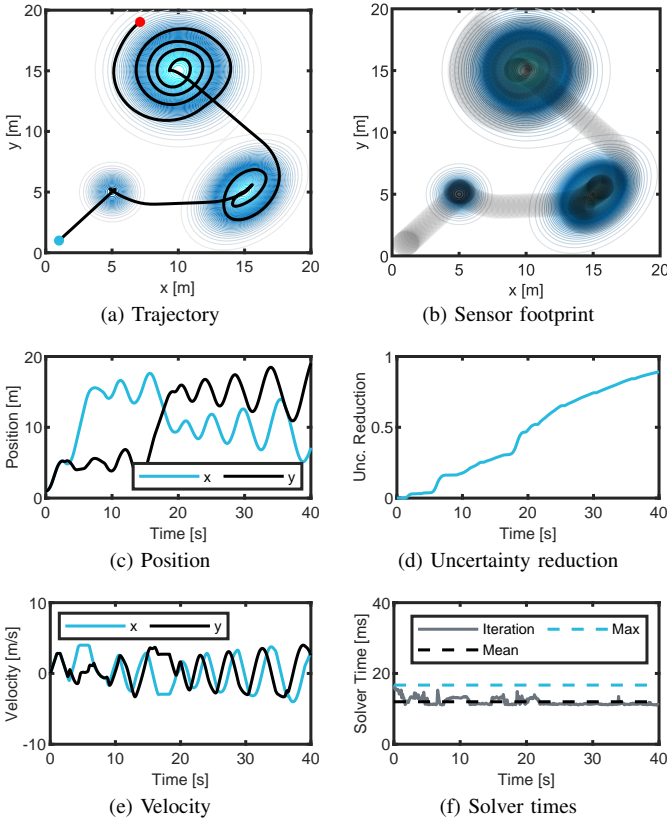


Fig. 11: Example where the uncertainty map comprises three components.

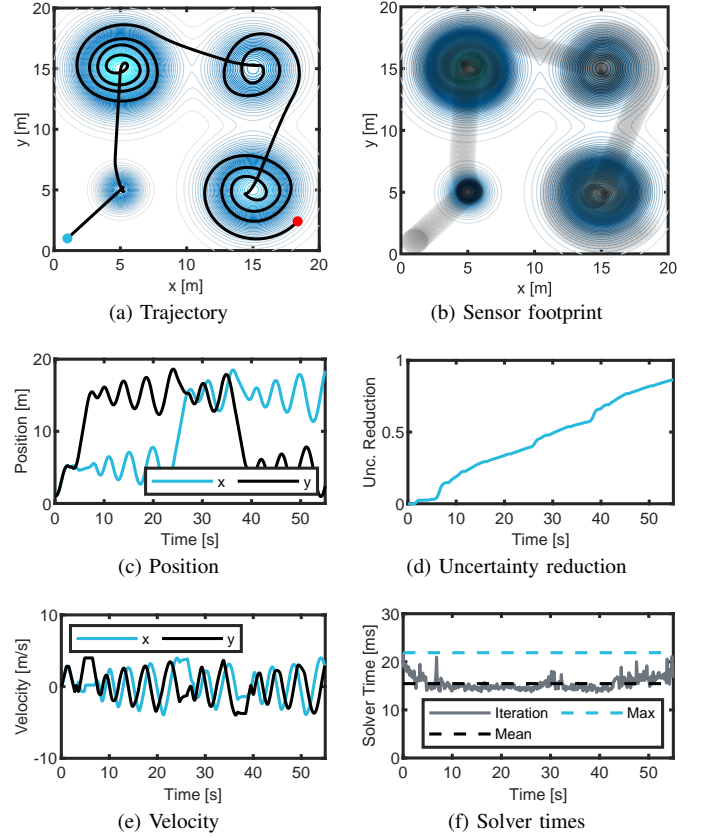


Fig. 12: Example with four radially symmetric Gaussian components.

B. Effect of the Weights

Since the objective function relies on the exponent α and the scaling coefficient λ , it is worth assessing how these parameters influence the algorithm. In this context, we consider the conditions of the initial example, where the uncertainty map comprises a single radially symmetric Gaussian, and we manipulate the weights λ and α . Fig.13 displays the resulting trajectories for distinct combinations of values of λ and α .

As λ decreases in value, less emphasis is placed on the penalty term. Consequently, the trajectories are expected to become more tightly concentrated, resulting in a greater overlap of the observation circles. This effect is noticeable in the examples depicted in Figs.13 (a) and 13 (b), and it becomes more pronounced when examining Fig. 14, which illustrates the coverage profiles for the various scenarios of Fig. 13. As shown in Fig. 14, there is a slower initial convergence in the scenario of Fig. 13 (b) when compared to Fig. 13 (a). However, at $t = 30$ s, both trajectories exhibit a similar coverage.

A similar impact can be anticipated when examining the variation of α . As α increases, the penalization becomes more pronounced, leading to a reduced overlap in the trajectories, which is observable in the examples of Figs. 13 (a) and 13 (d). Particularly, as illustrated in Fig. 14, one can notice that the trajectory in Fig. 13 (d) initially exhibits a quicker convergence when compared to that in Fig. 13 (a). However, at $t = 30$ s, the coverage obtained by the trajectory in Fig. 13 (a) is greater than that achieved by the trajectory of Fig. 13 (d). Ultimately, Fig. 13 (c) illustrates a scenario where α is sufficiently high to prevent the vehicle from executing a spiral curve.

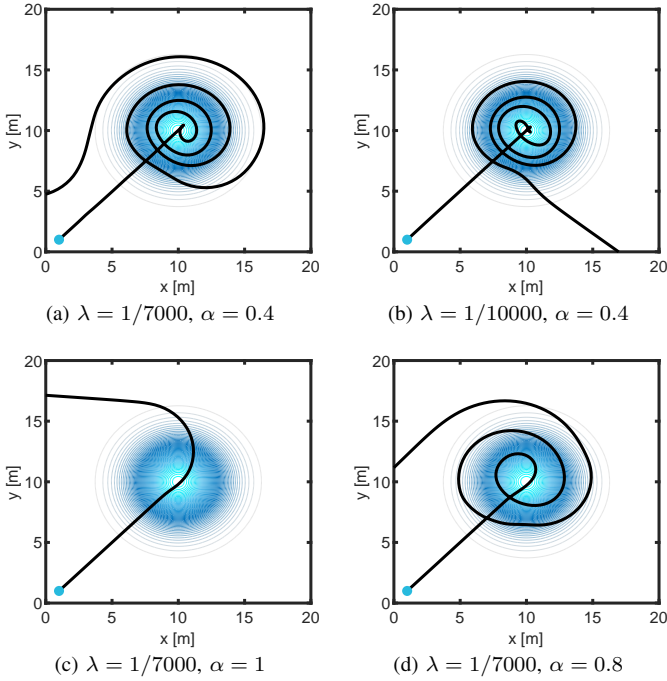


Fig. 13: Resulting trajectories for different combinations of λ and α .

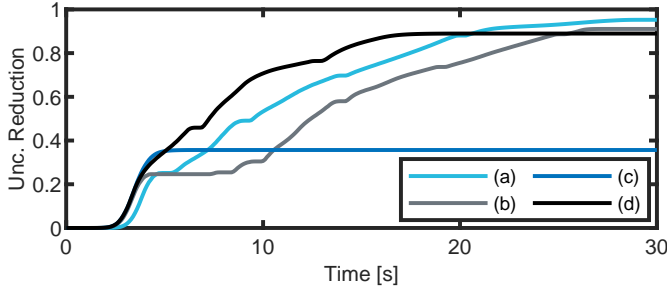


Fig. 14: Coverage profiles for the different combinations of λ and α .

Considering the previous discussion, it becomes clear that there is some need for parameter tuning associated with the proposed algorithm. Nevertheless, it should be acknowledged that the algorithm has the potential to be extended through the incorporation of variable weights. For instance, one could consider assigning higher penalties in regions where the uncertainty is higher, and lower penalties in regions where the uncertainty is lower. Moreover, one could employ decaying weights in the term \tilde{J}_k of the objective function to prioritize earlier prediction instants, potentially resulting in a faster convergence. Such variations of the algorithm could be easily incorporated, and a more exhaustive analysis could be performed. However, the decision to implement these variations is left as a user choice and may be a subject of consideration in future research.

C. Effect of the Horizon

It is also important to evaluate how the prediction horizon length impacts the performance of the proposed MPC algorithm. In this context, we begin our analysis by considering an uncertainty map comprising two Gaussian components, with Fig. 15 depicting the generated trajectories for two different prediction horizon lengths.

As illustrated in Fig. 15 (a), for a prediction horizon length of $N = 5$, the vehicle's predictive ability falls short and it is not able to predict the second Gaussian component. In contrast, when an extended horizon is employed, as shown in Fig. 15 (b) for $N = 15$, the vehicle is able to predict the second Gaussian component, leading to a trajectory that encompasses a greater volume of the uncertainty map. Therefore, it becomes apparent that, for each uncertainty function, there exists an approximate minimum horizon length that ensures the MPC algorithm is able to generate more efficient trajectories.

However, an extended horizon does not necessarily lead to higher-quality trajectories, as displayed in Fig. 16. Specifically, as shown in Fig. 16 (d), it becomes evident that the trajectories depicted in Figs. 16 (a) and 16 (b) produce similar coverage profiles, and, in fact, the trajectory from Fig. 16 (b) ultimately achieves a lower coverage than the trajectory in Fig. 16 (a). In addition, the trajectory in Fig. 16 (a) also exhibits a smoother profile than the one in Fig. 16 (b). Furthermore, it is important to highlight that a longer prediction horizon also results in an increased computational load, as demonstrated in Fig. 16 (c). In the context of this simple simulation, which lasts 30 seconds and features a single Gaussian component, for a horizon length of $N = 40$, each solver iteration already takes an average of approximately 35 ms. In contrast, for a horizon of $N = 15$, the average iteration time is only about 8 ms.

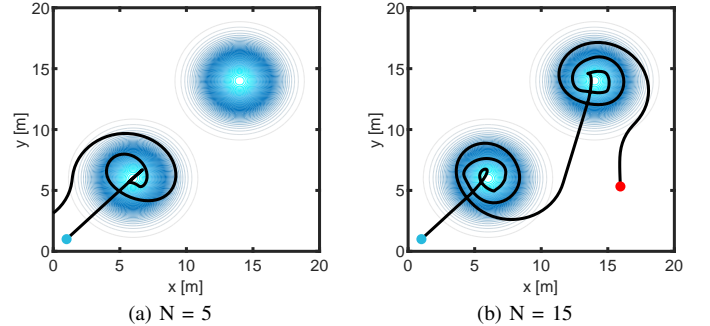


Fig. 15: Generated trajectories for two distinct prediction horizon lengths.

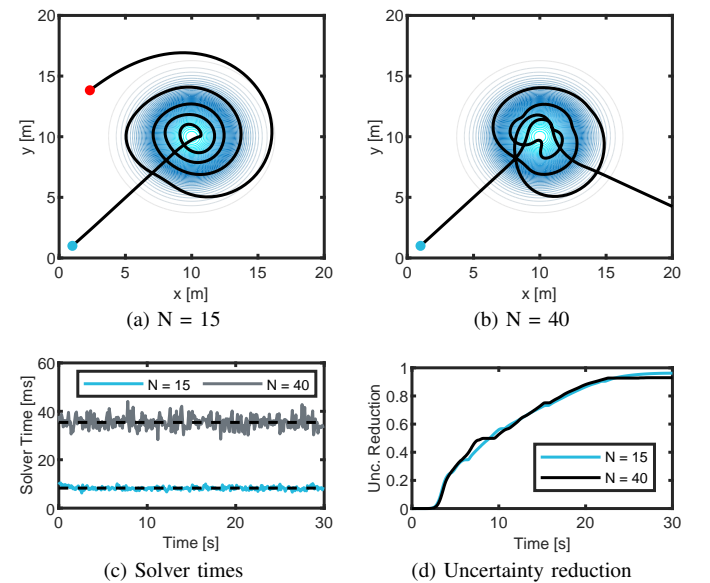


Fig. 16: Results obtained for different prediction horizon lengths.

D. Comparison with Victor Sierra Pattern

In this section, we perform a comparative analysis between the proposed algorithm and the Victor Sierra search pattern, a popular pattern that the US and Canadian coast guards employ in search and rescue missions. The Victor Sierra pattern, also known as Sector Search, is suitable for covering well-defined circular regions centered on a certain position. It consists of straight-line segments that form three equilateral triangular sectors, which are evenly distributed over the circular region. To consider the vehicle dynamics and ensure a more equitable comparison, we employ a standard MPC, subject to identical constraints, to guide the vehicle through the pattern by tracking each vertex in the prescribed sequence.

In Fig. 17, we present the resulting trajectories and covered regions obtained with the two methods for an uncertainty map composed of a single radially symmetric Gaussian. The Victor Sierra pattern was applied to the 95% confidence circle of the Gaussian component, resulting in the trajectory in Fig. 17 (b), and the proposed MPC algorithm produces the usual behavior, as depicted in Fig. 17 (a). As shown in Figs. 17 (c), 17 (d), and 18, there is a clear advantage in using the proposed algorithm, which is able to generate a trajectory that ultimately achieves a higher coverage, despite an initial slightly slower response.

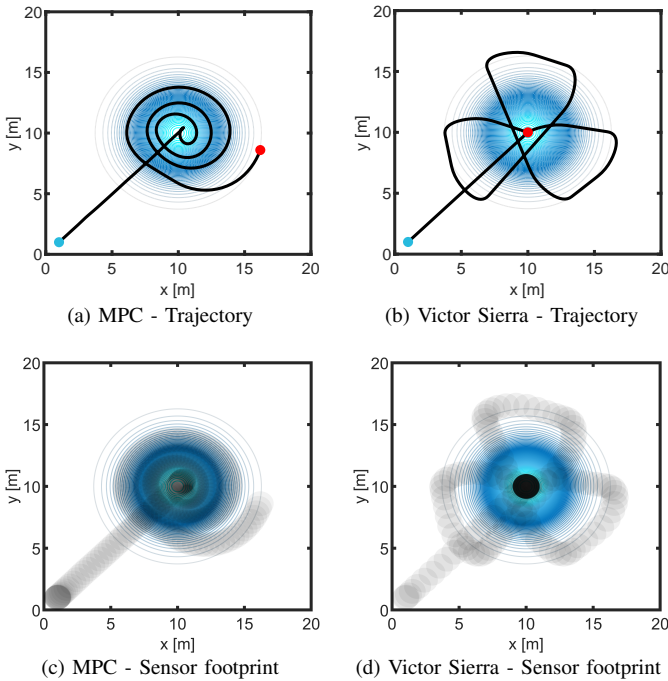


Fig. 17: Trajectories and sensor footprints generated by the two methods.

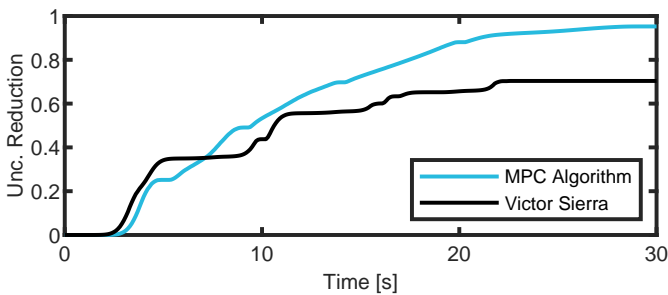


Fig. 18: Resulting coverage profiles for the two methods.

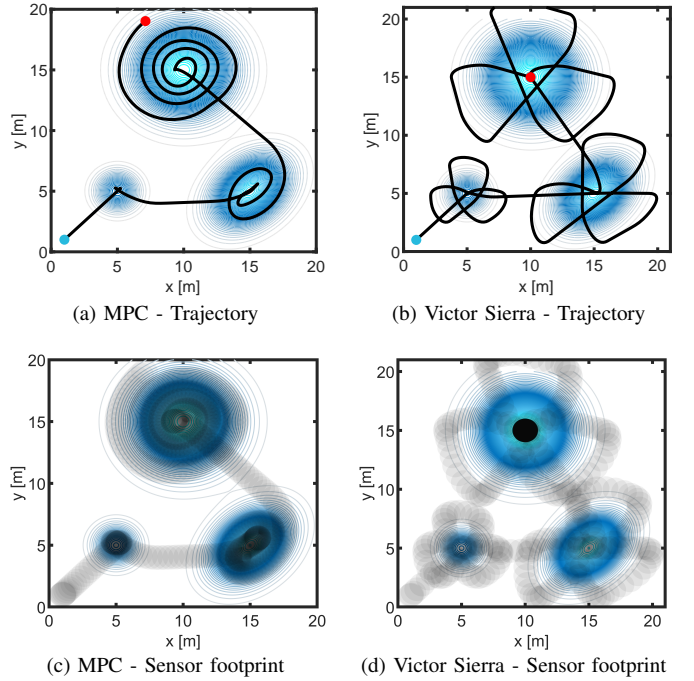


Fig. 19: Trajectories and sensor footprints generated by the two methods.

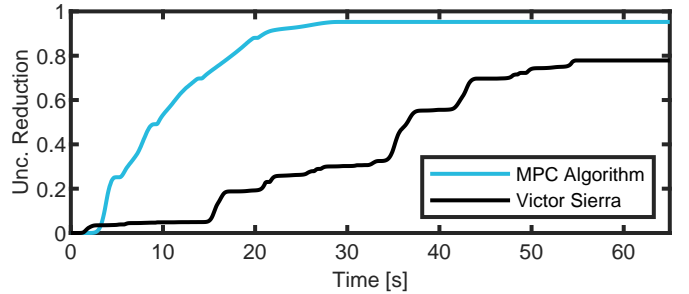


Fig. 20: Resulting coverage profiles for the two methods.

Additionally, we revisit the third example outlined in Section V-A, where the uncertainty map consists of three Gaussian components with distinct characteristics. In this scenario, we consider an extended version of the Victor Sierra pattern in which the pattern is applied individually to the 95% confidence ellipse of each component. This involves adjusting the pattern to the structure of each component through the relation that transforms a circle into an ellipse. Furthermore, to facilitate the comparison, the extended Victor Sierra pattern is applied to each component in an identical sequence to the one generated by the MPC algorithm. As displayed in Figs. 19 and 20, the MPC algorithm again produces a superior coverage profile compared to the adapted Victor Sierra pattern. This primarily occurs because, for components with smaller variances, the Victor Sierra introduces unnecessary redundancy, resulting in a slower response. Conversely, for components with higher variance, the pattern leaves uncovered areas, ultimately resulting in a reduced coverage compared to the MPC algorithm. It is important, however, to emphasize that arriving at a definitive conclusion is challenging, as the outcomes are contingent on various factors and parameters. Nonetheless, it is evident that the MPC algorithm is highly efficient and has the potential to surpass the Victor Sierra method.

VI. EXPERIMENTAL VALIDATION

In this section, the efficacy of the proposed MPC algorithm is assessed through simulations in the high-fidelity simulator Gazebo and by conducting actual experiments in an outdoor setting. The software used to perform simulations and conduct actual experiments in the quadrotor follows from the previous work done by Oliveira [21] and Jacinto [22]. The operating system consists of Ubuntu 20.04 along ROS melodic, and the MPC algorithm was implemented using the C++ CasADi API. Moreover, the Gazebo simulations were carried out using the Iris model, available through the PX4 Autopilot plugin, while the field trials were conducted with the M690B drone from a joint effort between FirePuma and Capture projects [23].

Concerning the Gazebo simulations, our initial approaches consisted in providing acceleration and, subsequently, velocity references to the PX4 low-level controller. Despite our efforts, these approaches posed challenges in achieving smooth and stable trajectories consistent with those obtained in MATLAB. Nonetheless, when commanding a complete trajectory generated offline, it yielded the anticipated outcomes, enabling the vehicle to follow the trajectories with minimal error.

Despite the lack of significant advantages in executing the algorithm online in this particular scenario, there is a natural desire to enable the real-time execution of the MPC algorithm to accommodate dynamic alterations in the future, like time-varying utility maps or obstacle avoidance. To enable the real-time execution of the algorithm and overcome the poor results obtained using lower-level references, we opted for a more conservative approach. The approach consists in commanding a given slice of the predicted optimal waypoint sequence to the PX4 controller. With such an approach, the penalty term of the objective function is still updated at each sampling time, but the optimization problem is only solved after the application of each waypoint sequence. This method ultimately produced results similar to those obtained by commanding a complete trajectory generated *a priori*.

A. Experimental Results

In the experiments presented in this section, the drone starts at $\mathbf{p} = [1 \ 1]^T$ with no initial velocity and the observation radius is assumed to be $r = 0.5$ m. In Gazebo, the algorithm operates with a sampling period of $T_s = 0.1$ s, a horizon length of $N = 20$, and the first 5 predicted optimal waypoints are sent to the PX4 controller. Consequently, the optimization problem is solved from 0.5 s to 0.5 s. The MPC is warm-started using the shifting method but by shifting 5 steps. Moreover, the MPC considers a max velocity of 2 m/s and a max acceleration of 2 m/s² for the drone. Regarding the field tests, due to difficulties faced when attempting to execute the algorithm onboard, the field trials were carried out by instructing waypoints generated *a priori* under identical conditions.

We begin by considering an example where the uncertainty map is composed of a single radially symmetric component, with the corresponding results displayed in Fig. 21. As illustrated in Fig. 21 (a), the drone exhibits the expected behavior in the Gazebo simulation, executing a smooth spiral curve, as also reflected in the position profiles shown in Fig. 21 (e). Such

behavior is obviously possible due to the appropriately tuned parameters of the MPC, which allow the generation of smooth trajectories that the PX4 controller can track efficiently. In addition, as depicted in Fig. 21 (g), the computational times are also sufficiently fast to allow for a good performance, with each solver iteration taking approximately 18 ms on average.

Concerning the field trial, as shown in Fig. 21 (b), it can be observed that the resulting trajectory is not as consistent as the one from the Gazebo simulation. This discrepancy primarily arises from the influence of wind disturbances encountered in the outdoor experimental environment. In addition, there are also some inaccuracies associated with the Global Positioning System (GPS) of the drone, structural differences between the drones used in Gazebo and in the real trials, and differences in the tuning of the PX4 inner-loop controllers. Nevertheless, for the designated observation radius, both trajectories show a similar coverage by the final instant, as shown in Fig. 21 (h).

To conclude, we present an example where the uncertainty map comprises five Gaussian components, with Fig. 22 displaying the results obtained in Gazebo and in the corresponding experimental test. As illustrated in Fig. 22 (a), the map comprises four circular Gaussian components. Two of these components have relatively small variances in comparison to the vehicle's observation radius, while the other two exhibit higher variances. Additionally, there is a fifth component with an elliptical shape, and its variance along one of its axes is small when compared to the observation radius of the drone.

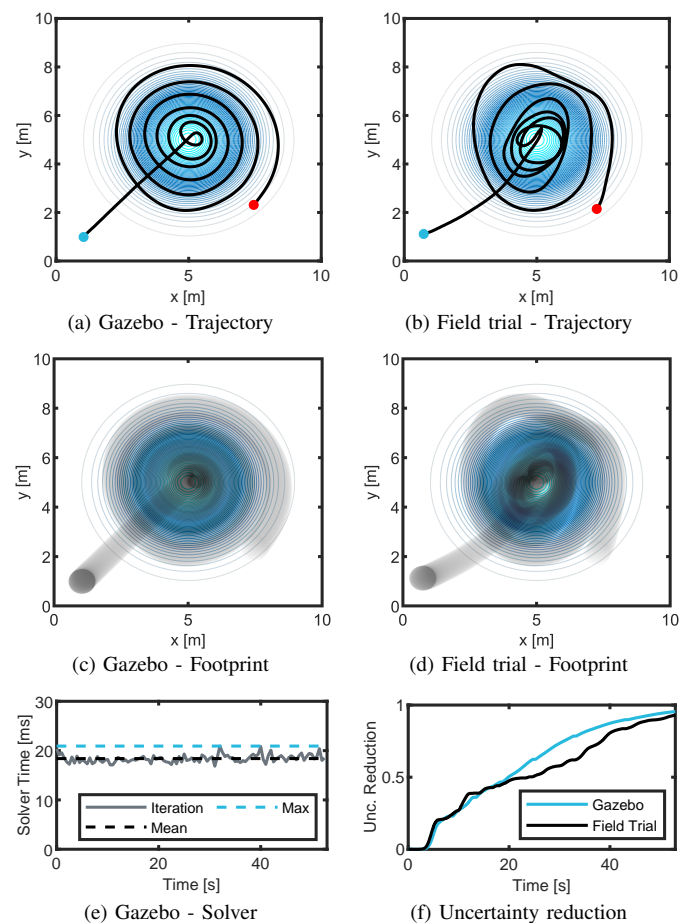


Fig. 21: Gazebo and field trial results for a simple uncertainty map.

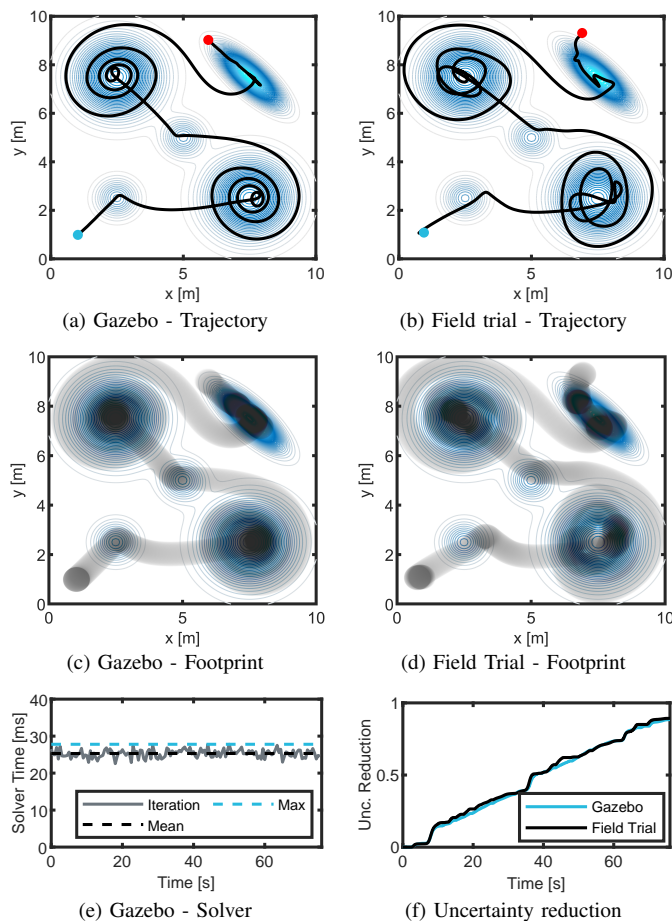


Fig. 22: Results for an uncertainty map comprising five Gaussian components.

In particular, we draw attention to the vehicles's behavior when analyzing the fifth component, in which case the drone follows a straight path along the major axis of the Gaussian. In addition, we draw attention to Fig. 22 (g), which shows that each solver iteration now takes approximately 25 ms on average. Ultimately, we highlight that the field trial results are comparable to the Gazebo simulation.

VII. CONCLUSION & FUTURE RESEARCH

This paper tackles the trajectory planning problem for UAV search and coverage missions based on a utility map described as a linear combination of Gaussian distributions. We propose an MPC algorithm that promotes the exploration of the map by preventing the vehicle from revisiting previously covered regions. This is achieved by penalizing intersections between the circular observation regions along the vehicle's trajectory. Due to the complexity of precisely determining the intersection area between two circles, we introduce an exponential penalty function. The algorithm is tested in MATLAB, Gazebo, and in outdoor trials. The results show that the algorithm can generate efficient trajectories for search and coverage missions.

Possible extensions involve developing a subroutine to reduce the number of components in the penalty term and generalizing the algorithm by using variable weights to finetune its performance. Since we assumed a static utility map, future research may also focus on the search and coverage problem based on time-varying utility functions.

REFERENCES

- [1] H. Shakhathreh, A. H. Sawalmeh, A. Al-Fuqaha, Z. Dou, E. Almaita, I. Khalil, N. S. Othman, A. Khreishah, and M. Guizani, "Unmanned aerial vehicles (UAVs): A survey on civil applications and key research challenges," *IEEE Access*, vol. 7, pp. 48572–48634, 2019.
- [2] M. Ghamari, P. Rangel, M. Mehrubeoglu, G. S. Tewolde, and R. S. Sherratt, "Unmanned aerial vehicle communications for civil applications: A review," *IEEE Access*, vol. 10, pp. 102492–102531, 2022.
- [3] P. Yao, Z. Xie, and P. Ren, "Optimal UAV route planning for coverage search of stationary target in river," *IEEE Transactions on Control Systems Technology*, vol. 27, no. 2, pp. 822–829, 2017.
- [4] F. Afghah, A. Razi, J. Chakareski, and J. Ashdown, "Wildfire monitoring in remote areas using autonomous unmanned aerial vehicles," in *IEEE INFOCOM 2019-IEEE Conference on Computer Communications Workshops (INFOCOM WKSHPs)*, pp. 835–840, IEEE, 2019.
- [5] N. Nigam, S. Bieniawski, I. Kroo, and J. Vian, "Control of multiple UAVs for persistent surveillance: Algorithm and flight test results," *IEEE Transactions on Control Systems Technology*, vol. 20, no. 5, pp. 1236–1251, 2011.
- [6] E. M. Lee, J. Choi, H. Lim, and H. Myung, "Real: Rapid exploration with active loop-closing toward large-scale 3d mapping using uavs," in *2021 IEEE/RSJ International Conference on Intelligent Robots and Systems (IROS)*, pp. 4194–4198, IEEE, 2021.
- [7] E. Galceran and M. Carreras, "A survey on coverage path planning for robotics," *Robotics and Autonomous systems*, vol. 61, no. 12, pp. 1258–1276, 2013.
- [8] T. M. Cabreira, C. Di Franco, P. R. Ferreira, and G. C. Buttazzo, "Energy-aware spiral coverage path planning for uav photogrammetric applications," *IEEE Robotics and automation letters*, vol. 3, no. 4, pp. 3662–3668, 2018.
- [9] M. Torres, D. A. Pelta, J. L. Verdegay, and J. C. Torres, "Coverage path planning with unmanned aerial vehicles for 3D terrain reconstruction," *Expert Systems with Applications*, vol. 55, pp. 441–451, 2016.
- [10] E. U. Acar, H. Choset, and J. Y. Lee, "Sensor-based coverage with extended range detectors," *IEEE Transactions on Robotics*, vol. 22, no. 1, pp. 189–198, 2006.
- [11] Y. Jia, S. Zhou, Q. Zeng, C. Li, D. Chen, K. Zhang, L. Liu, and Z. Chen, "The UAV Path Coverage Algorithm Based on the Greedy Strategy and Ant Colony Optimization," *Electronics*, vol. 11, no. 17, p. 2667, 2022.
- [12] M.-H. Kim, H. Baik, and S. Lee, "Response threshold model based UAV search planning and task allocation," *Journal of Intelligent & Robotic Systems*, vol. 75, pp. 625–640, 2014.
- [13] E. J. Forsmo, E. I. Grøtli, T. I. Fossen, and T. A. Johansen, "Optimal search mission with unmanned aerial vehicles using mixed integer linear programming," in *2013 International conference on unmanned aircraft systems (ICUAS)*, pp. 253–259, IEEE, 2013.
- [14] P. Yao, H. Wang, and H. Ji, "Gaussian mixture model and receding horizon control for multiple uav search in complex environment," *Nonlinear Dynamics*, vol. 88, pp. 903–919, 2017.
- [15] J. Lofberg, "Yalmip: A toolbox for modeling and optimization in matlab," in *2004 IEEE international conference on robotics and automation (IEEE Cat. No. 04CH37508)*, pp. 284–289, IEEE, 2004.
- [16] R. Mahony, V. Kumar, and P. Corke, "Multirotor aerial vehicles: Modeling, estimation, and control of quadrotor," *IEEE robotics & automation magazine*, vol. 19, no. 3, pp. 20–32, 2012.
- [17] "PX4 Autopilot User Guide". Available online: PX4 Autopilot.
- [18] J. Andersson, J. Åkesson, and M. Diehl, "Casadi: A symbolic package for automatic differentiation and optimal control," in *Recent advances in algorithmic differentiation*, pp. 297–307, Springer, 2012.
- [19] A. Wächter and L. T. Biegler, "On the implementation of an interior-point filter line-search algorithm for large-scale nonlinear programming," *Mathematical programming*, vol. 106, pp. 25–57, 2006.
- [20] S. Gros, M. Zanon, R. Quirynen, A. Bemporad, and M. Diehl, "From linear to nonlinear mpc: bridging the gap via the real-time iteration," *International Journal of Control*, vol. 93, no. 1, pp. 62–80, 2020.
- [21] T. Oliveira, P. Trindade, D. Cabecinhas, P. Batista, and R. Cunha, "Rapid development and prototyping environment for testing of unmanned aerial vehicles," in *2021 IEEE International Conference on Autonomous Robot Systems and Competitions (ICARSC)*, pp. 191–196, IEEE, 2021.
- [22] M. Jacinto, R. Cunha, and A. Pascoal, "Chemical spill encircling using a quadrotor and autonomous surface vehicles: A distributed cooperative approach," *Sensors*, vol. 22, no. 6, p. 2178, 2022.
- [23] M690B Wiki. Available online: M690B Wiki.